Journal of Advanced Ceramics
2020, **9**(2): 162–172
https://doi.org/10.1007/s40145-019-0356-y
ISSN 2226-4108
CN 10-1154/TQ

Research Article

Effects of calcination temperature and time on the $Ca_3Co_4O_9$ purity when synthesized using starch-assisted sol–gel combustion method

M. A. MOHAMMED[a,c], M. B. UDAY[a,b], S. IZMAN[a,*]

[a]*School of Mechanical Engineering*, *Faculty of Engineering*, *Universiti Teknologi Malaysia (UTM)*, *UTM Skudai 81310*, *Johor*, *Malaysia*
[b]*Centre for Advanced Composite Materials (CACM)*, *Institute for Vehicle Systems and Engineering*, *Universiti Teknologi Malaysia*, *UTM Skudai 81310*, *Johor*, *Malaysia*
[c]*Department of Materials Engineering*, *College of Engineering*, *University of Basrah*, *Basrah*, *Iraq*

Received: October 6, 2019; Revised: November 13, 2019; Accepted: November 27, 2019

Abstract: $Ca_3Co_4O_9$ is a p-type semiconducting material that is well-known for its thermoelectric (TE), magnetic, electronic, and electro-optic properties. In this study, sol–gel autoignition was used to prepare $Ca_3Co_4O_9$ at different calcination temperatures (773, 873, 973, and 1073 K) and time (4, 6, 8, 10, 12, and 14 h) using starch as a fuel. The phase and microstructure of the prepared $Ca_3Co_4O_9$ powder were investigated. Thermogravimetry–differential thermal analysis (TGA) confirms that the final weight loss occurred at 1073 K to form $Ca_3Co_4O_9$ stable powder. The variable-pressure scanning electron microscopy (VP-SEM) images show that the size of powder particles increases from 1.15 to 1.47 μm as calcination time increases from 4 to 12 h, and the size remains almost constant thereafter. A similar pattern is also observed on the increment of the crystallite size and percentage of crystallinity with X-ray diffraction (XRD) analysis. The highest crystallinity is found about 92.9% when the powder was calcinated at 1073 K for 12 and 14 h with 458 and 460 Å crystallite size, respectively. Energy dispersive X-ray spectroscopy (EDS) analysis demonstrates that the calcinated powder has a high intensity of Ca, Co, and O with uniform distribution. High-resolution transmission electron microscopy (HRTEM) images prove that there is no distinct lattice distortion defect on the crystal structure.

Keywords: calcium cobalt oxide; sol–gel; starch; combustion method; crystallite size; crystallinity

1 Introduction

In recent years, utilizing of fossil fuels has shown severe impacts on atmospheric and environmental problems, causing international warming, climate change, greenhouse gas emission, ozone layer depletion, and acid rain. The thermoelectric power generator is one of the promising ways to reduce dependency on fossil fuels to generate energy. Thermoelectric devices can generate electrical energy from waste heat, and they are a highly encouraging solution for waste heat recovery and self-powered systems [1–3]. The oxide-based thermoelectric material can be utilized at high temperature in an oxidizing environment. In addition, these materials are nontoxic and having low processing cost, thermal, and

* Corresponding author.
E-mail: izman@utm.my

chemical stability. Therefore, they have been recognized as promising thermoelectric materials [4]. However, despite of these advantages, the disadvantage of thermoelectric oxides is their low efficiency (figure of merit). Therefore, these oxides need to improve their thermoelectric properties to enhance the thermoelectric conversion efficiency.

The misfit of calcium cobalt oxide ($Ca_3Co_4O_9$) ceramics is eliciting considerable interest for their practical applications in refrigeration devices, recycling of waste heat to electricity, and solar thermoelectric generators [5]. Calcium cobaltite is also extensively studied as a possible thermoelectric oxide material due to its low electrical resistivity and high Seebeck coefficient with low thermal conductivity [6,7]. Therefore, in most thermoelectric applications, doping of $Ca_3Co_4O_9$ ceramics to increase electric conductivity is indispensable. Many kinds of research have been conducted to evaluate the effects of various doping and co-doping elements on the changes of crystal structure and thermoelectric properties of the material. For instance, in the recent developments, significant enhancement in the thermoelectric performance of $Ca_3Co_4O_9$ thermoelectric material was reported through combined strontium substitution and hot-pressing process [8]. While in Ref. [9], Na and W dual doping in $Ca_3Co_4O_9$ system was claimed able to increase figure of merit value more than two times of the undoped sample at 1000 K. The crystal structure of $Ca_3Co_4O_9$ misfit-layered as shown in Fig. 1 consists of two layers $(Ca_2CoO_3)(CoO_2)_{b_1/b_2}$. The Ca_2CoO_3 layer is an insulating distorted NaCl type, and the CoO_2 layer is an electrically conductive CdI_2 type. They stack along the *c*-axis alternately, with b_1 and b_2 representing the length of the (Ca_2CoO_3) and (CoO_2) sublattice, respectively, along the *b*-axis [10,11]. The Ca_2CoO_3 layer decreases the thermal conductivity due to work as phonon scattering centers, whereas the CoO_2 layer serves as electron transport sites due to having an effectively correlated electron system [7].

Several synthesis methods have been used to produce $Ca_3Co_4O_9$ powder, including thermal hydro-decomposition [15], pechini [16], polymer solution synthesis [17], and solid-state reaction [18–22]. These processes are operating at high reaction temperatures, long process, and low chemical homogeneity [23]. Apart from powder synthesis, only solid-state reaction technique has reported the effect of calcination procedure, temperature, and time on thermoelectric properties. For instance, Smaczyński *et al*. [24] studied the influence of the solid-state reaction and calcination at different temperatures and time using the thermogravimetry–differential thermal analysis (TGA) test. The results showed that a stable composition of $Ca_3Co_4O_9$ powder was obtained at calcination at 1073 K for a higher soaking time between 20 and 30 h. However, some traces of cobalt oxide were still observed in the calcinated powder because of the $Ca_3Co_4O_9$ nonstoichiometry at room temperature. Bresch *et al*. [25] investigated the effect of the calcination procedure on the thermoelectric properties of $Ca_3Co_4O_9$ powder using solid-state reaction technique. According to this study, no systematic study had been done on the thermoelectric properties affected by the calcination procedure. Conversely, the advantages of sol–gel combustion method are simple, easy control of homogeneity and stoichiometry, and

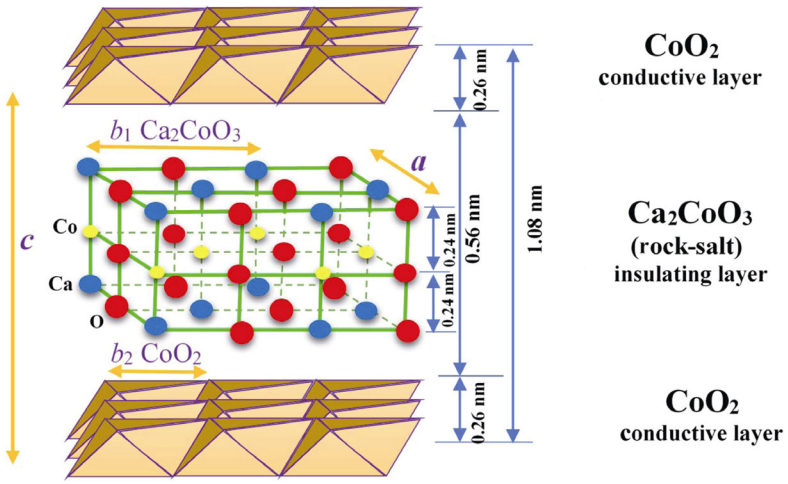

Fig. 1 Crystal structure of $Ca_3Co_4O_9$ [12–14]. Reproduced with permission from Ref. [12], © Elsevier Ltd and Techna Group S.r.l. 2018; Ref. [13], © The Royal Society of Chemistry. 2016; and Ref. [14], © American Chemical Society. 2016.

economical preparation [26,27]. Previous studies showed that synthesized $Ca_3Co_4O_9$ powder produced by the sol–gel method results in fine-sized particles, as well as regular size distribution, which is significant in improving magnetic, electrical, and optical properties [12,28–31].

In the sol–gel preparation method, ethylene glycol, polyethylene glycol, and nitric acid were used to polymerize the solution, induce nitrate salt decomposition, and facilitate new compound formation [32,33]. On the other hand, citric acid and polyethylene glycol were used to polymerize the solution which produces carbonaceous xerogel and needs to be crushed [3,31, 34–36]. Some researchers focused on the preparation of $Ca_3Co_4O_9$ powder with different calcination conditions by using different preparation techniques. For example, Chen *et al*. [7] investigated the influence of the precursor calcination temperature on the microstructure properties of $Ca_3Co_4O_9$ powder. They prepared the calcium cobaltite powder using the sol–gel technique and calcined at various temperatures between 923 and 1073 K. The results showed that the calcination temperature has a significant effect on the microstructure properties. Crystal size increases with the increase in the calcination temperature. However, they did not study the effect of calcination time on the crystallite size.

Most of polymerizing agents used in powder preparation are acid-based which require special care in handling them for preparing ceramic powder. Recent developments show that starch has been increasingly used as a fuel in the sol–gel combustion method [37–43] due to the ease of preparation and environmental friendliness. Apart from that, it only generates CO_2, N_2, and H_2O after ignition [44,45]. Moreover, the use of starch as a fuel is becoming more favorable because its ability to maintain the pH of the gel [46,47] and it generates non-toxic gases during the calcination process. The method is also capable of producing nanoparticle powder with pure phase [37–39,44,48] and homogenous doped particles [37]. It has been reported that the thermoelectric properties improve with smaller powder grain size, which exhibits low thermal conductivity [49,50]. Previous investigations on the properties of $Ca_3Co_4O_9$ powder using starch as fuel were only limited to the preparation of powder at different temperatures [45]. However, there is no report published on the effect of calcination time on the particle size, crystallite size, and crystallinity as yet. The aim of the present study is to evaluate the microstructure of $Ca_3Co_4O_9$ powder when it is prepared via the sol–gel combustion method and uses starch as a fuel during the calcination process.

2 Materials and experiments

Polycrystalline $Ca_3Co_4O_9$ powder was synthesized using the sol–gel combustion method. Starch $(C_6H_{10}O_5)_n$ was used as a combustion fuel and gelling agent. Calcium nitrate tetrahydrate $Ca(NO_3)_2{\cdot}4H_2O$ (99%) and cobalt nitrate hexahydrate $Co(NO_3)_2{\cdot}6H_2O$ (99%) were dissolved in distilled water and stirred using a magnetic hot-plate stirrer (IKA-C-MAG HS4, Germany) to obtain a stoichiometric mixture. The starch was mixed with distilled water, and the solution was added gradually into the mixed metal–nitrate solution. The produced transparent pink solution was heated under constant stirring within 353–373 K to obtain a pink gel. Subsequently, the resultant gel was decomposed using a hot-plate at 673 K for 1 h, and stirred until the gel burned and became a black precursor. TGA of the precursor was carried out using TA instruments Q500 TGA (Leatherhead, UK) from room temperature to 1383 K in the air at a heating rate of 10 ℃/min. The precursor was then calcined at different temperatures (773, 873, 973, and 1073 K) and time (4, 6, 8, 10, 12, and 14 h) at a heating rate of 10 ℃/min under ambient using Carbolite CWF 12/23 electric furnace. The morphology of $Ca_3Co_4O_9$ particles was examined using a variable-pressure scanning electron microscope (Model-JEOL JSM-IT300LV) and energy dispersive X-ray spectroscope (JEOL JSM-IT300LV, Akishima, Japan) for elemental mapping. The crystal structures of calcined $Ca_3Co_4O_9$ particles powdered at different dwelling times were characterized using a Rigaku (Smartlab) X-ray diffractometer with Cu Kα radiation (λ = 0.154, 18 nm) and 2θ value was between 5° and 60°. The lattice structure of $Ca_3Co_4O_9$ powder was examined under scanning transmission electron microscopy (STEM) with a JEOL JEM-ARM200F (FEG-STEM/TEM- USA model) at 200 kV with a 0.08 nm resolution, equipped with a Cs-corrector (CEOS GmbH) for the electron probe.

3 Results and discussion

The black precursor was obtained after the pink gel heated at 673 K for 1 h. The conversion process of the

gel is represented by Eq. (1). The synthesized black precursor was then studied using TGA, and the results are shown in Fig. 2. It illustrates the weight loss percentage as a function of temperature for the $Ca_3Co_4O_9$ sample. The TGA curves show that the $Ca_3Co_4O_9$ powder is stable up to 860 K, and no weight loss is observed below this temperature. The maximum weight loss peak occurred at 973 K as a result of $Ca_3Co_4O_9$ compound formation, partially (CaO and Co_3O_4) from the decomposition of calcium carbonate into calcium oxide by the release of carbon dioxide (CO_2). The weight loss process is represented by Eq. (2). The final weight loss occurred at 1073 K, where the decomposition residuals of cobalt oxide and calcium oxide formed a stable $Ca_3Co_4O_9$ product. Equation (3) explains the weight loss due to $Ca_3Co_4O_9$ compounds formed. These results are in agreement with Refs. [45,51,52].

$$[9Ca(NO_3)_2\cdot 4H_2O+12Co(NO_3)_2\cdot 6H_2O+n(C_6H_{10}O_5)]_{gel} \xrightarrow{673\ K} [9CaCO_3+4Co_3O_4]_{black\ precursor} + n[N_{2(g)}+CO_{2(g)}+H_{2(g)}] \quad (1)$$

$$CaCO_3+Co_3O_4+O_2 \xrightarrow{973\ K} Ca_3Co_4O_9 + m[CaO+Co_3O_4]+n[CO_{2(g)}+H_{2(g)}] \quad (2)$$

$$9CaO+4Co_3O_4 \xrightarrow{1073\ K} 3Ca_3Co_4O_9+n[O_{2(g)}] \quad (3)$$

Figure 3(a) shows the image of black powder formed after pink gel burnt at 673 K for 1 h. Figures 3(b)–3(e) illustrate the morphology of black powder after being calcinated at 773, 873, 973, and 1073 K for 4 h, respectively. As the calcination temperature increases, the size of black powder particles also increases, and the shape of particles becomes more defined at 1073 K.

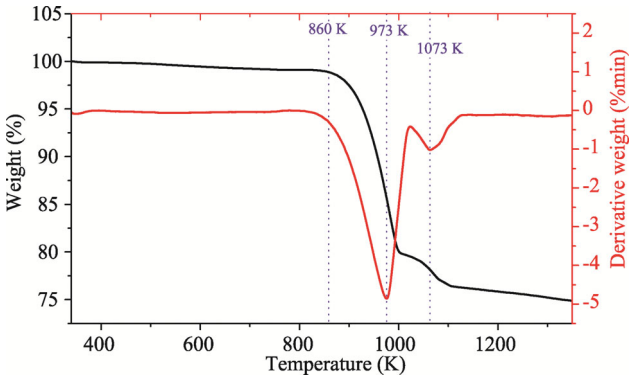

Fig. 2 TGA of $Ca_3Co_4O_9$ powder.

Figure 4 demonstrates the X-ray diffraction (XRD) results of each calcinated powder. At low calcinated temperatures (< 973 K), the $CaCO_3$ and Co_3O_4 phases are dominant while $Ca_3Co_4O_9$ phase only appears marginally at 873 K. The amorphous phase of $Ca_3Co_4O_9$ formed at 973 K, and single phase of $Ca_3Co_4O_9$ only becomes more evident at 1073 K.

Figures 5(a)–5(f) show scanning electron micrographs of the $Ca_3Co_4O_9$ powder when calcined at 1073 K at different calcination dwelling time (4, 6, 8, 10, 12, and 14 h), respectively. The images reveal that the

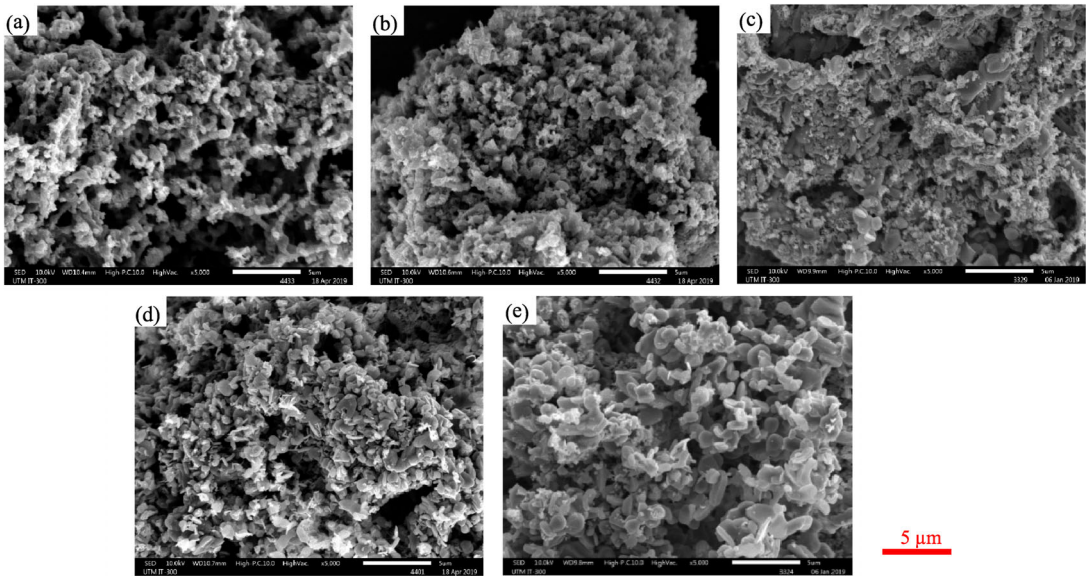

Fig. 3 VP-SEM micrographs of black powder (a) before calcination; after calcination for 4 h at (b) 773, (c) 873, (d) 973, and (e) 1073 K.

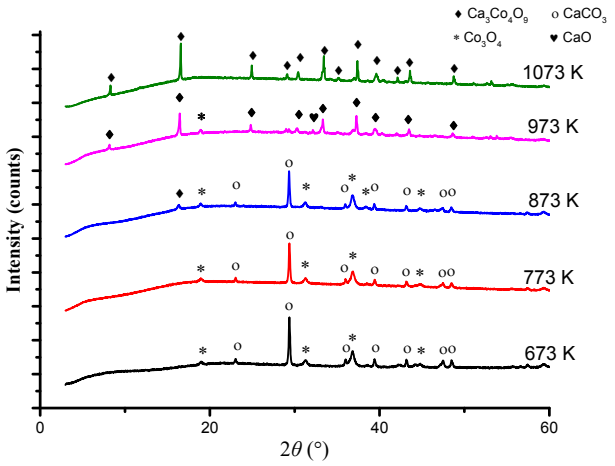

Fig. 4 XRD patterns of black powder before calcination and after calcinated for 4 h at 773, 873, 973, and 1073 K.

calcination time has an effect on the particle size distribution and morphology of these particles. The calcined $Ca_3Co_4O_9$ powder demonstrates a fine particle size with plate-like as well as irregular shape morphology. The distribution of particles size is quite homogenous and normally distributed as shown in Figs. 5(g)–5(l) with a mean of 1.15, 1.19, 1.38, 1.39, 1.47, and 1.47 μm for 4, 6, 8, 10, 12, and 14 h calcination time, respectively. The morphology of the powder has changed slightly with increasing the average particle size, and some agglomerations were observed between fine particles. The number of plate-like shaped particles increased with the increase of calcination time, which is due to the grain growth over the soaking time.

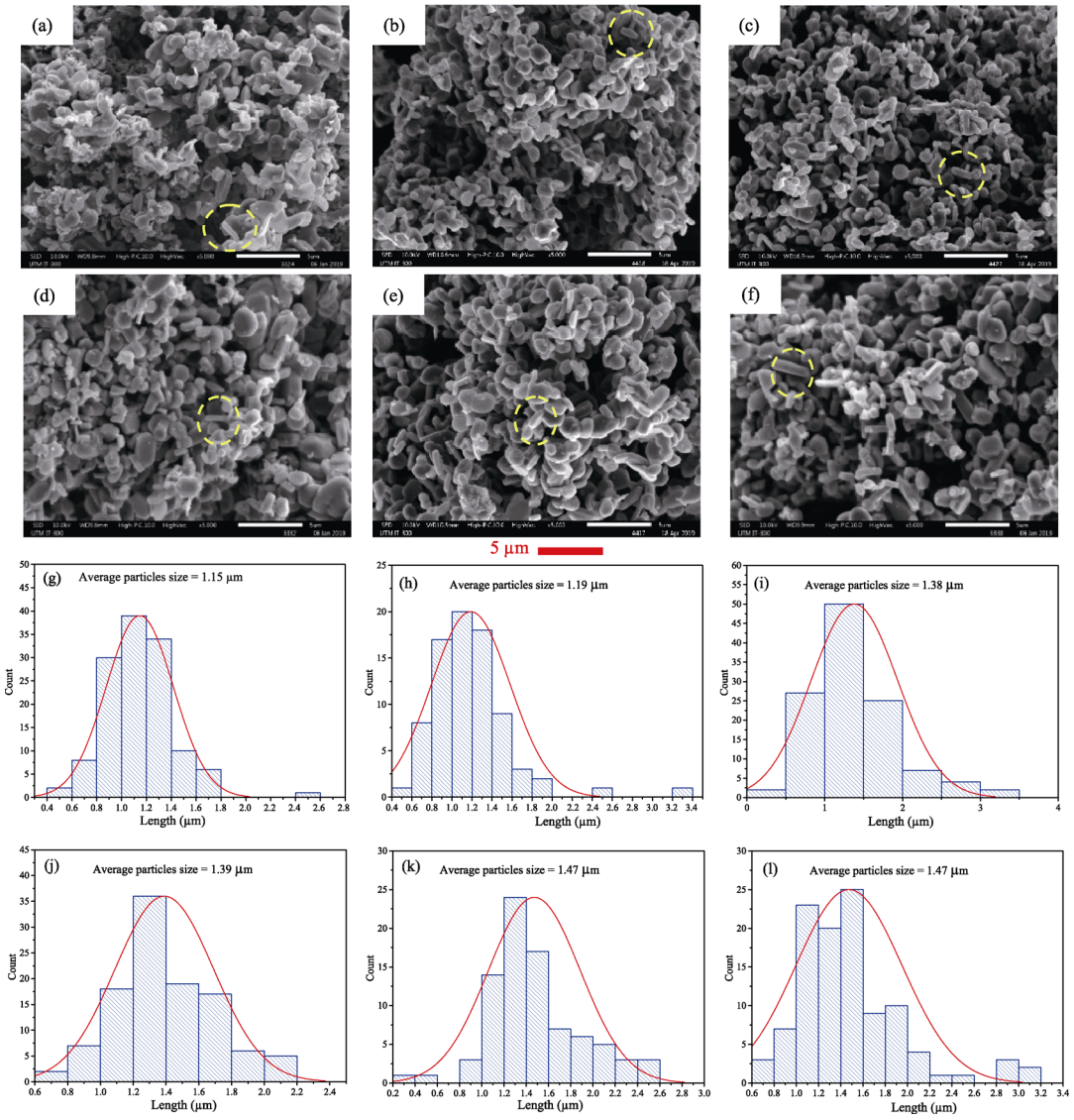

Fig. 5 VP-SEM micrographs of $Ca_3Co_4O_9$ powder calcined at 1073 K with different calcination time (a) 4, (b) 6, (c) 8, (d) 10, (e) 12, and (f) 14 h and their particle size distribution in (g–l), respectively. Yellow circles indicate plate-like particles.

The effect of calcination time on lattice-parameters was analyzed using XRD patterns on the powder calcined at 1073 K. These XRD patterns are shown in Fig. 6(a). All peaks were indexed according to ICDD PDF card number 00-021-0139. Structural parameters were refined with the superspace group X2/m(0b0)s0 using JANA 2006 software [53]. The refined XRD pattern of 12 h calcination time sample is shown in Fig. 6(b), as an example. Miller indices are also illustrated in Fig. 6(a) and all the peaks determine the transformation of $Ca_3Co_4O_9$ powder to the monoclinic misfit crystal structure. The lattice parameters were estimated based on the XRD patterns of each powder, as summarized in Table 1. The crystal parameters a = 4.835 , b_1 = 4.556, b_2 = 2.824, c = 10.854, and b_1/b_2 ratio of 1.613 for the 12 h-calcined powder were close to the crystal parameters as reported by Masset *et al.* [10,54–56]. From XRD data, the analysis of the crystallite size of $Ca_3Co_4O_9$ nanocrystals was calculated using a modified Scherer equation as follows:

$$D = K\lambda / \beta\cos\theta \tag{4}$$

where D is the crystallite size (nm), K is a shape factor, which usually takes a value of about 0.9, λ is the wavelength of X-ray source for Cu Kα radiation (λ = 0.15418 nm), β is the full width at half-maximum (FWHM) of the observed peak, and θ is the Bragg diffraction angle (°) [38,57–59].

The crystallinities of $Ca_3Co_4O_9$ powder were calculated from the XRD intensity data by assuming a two-phase structure (crystalline–amorphous) with a line through the minimum intensity to get an arbitrary background to diffraction trail, thus an arbitrary crystalline phase segregating from an amorphous phase [43,44]. The crystallinity X_{cr} was calculated by the following equation:

$$X_{cr} = \frac{A_{cr}}{A_{cr} + A_{am}} \times 100\% \tag{5}$$

where A_{cr} and A_{am} are the integrated areas of the crystalline and amorphous phases, respectively. Figure 7 illustrates the relationship of the calcination time with the degree of crystallinity and crystallite size of the synthesized $Ca_3Co_4O_9$. It can be seen that the degree of crystallinity and crystallite size increase with the increasing of calcination time. As the calcination time increases, the crystallinity of $Ca_3Co_4O_9$ powder improves near to 92.9%, and it becomes less amorphous. The application of TE materials requires pure phase and thermally stable bulk materials [60]. It is noticed that the crystallite size and crystallinity (%) of powder become insensitive after 12 h calcination time.

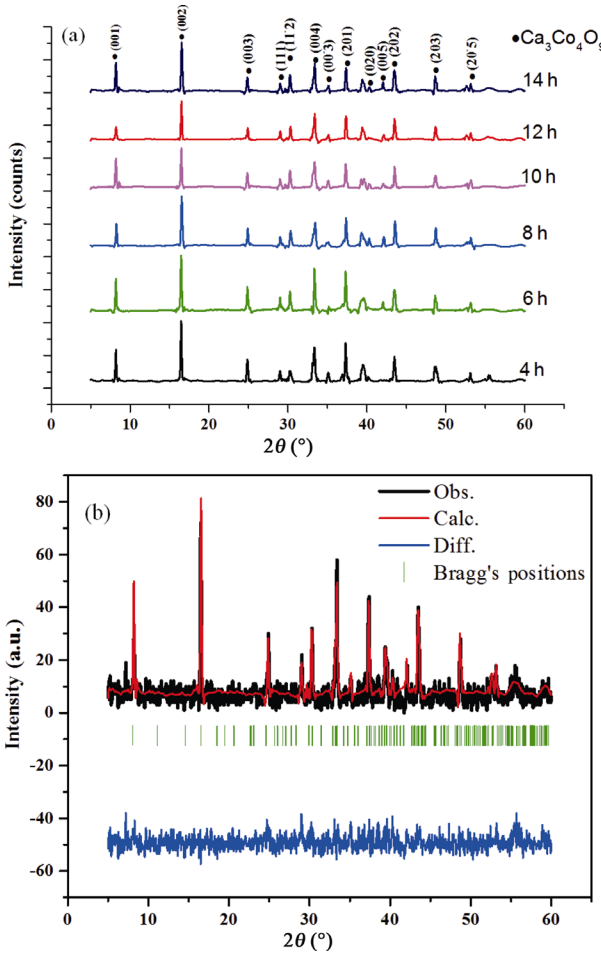

Fig. 6 (a) XRD patterns of pure $Ca_3Co_4O_9$ powder calcinated at 1073 K with different time of 4, 6, 8, 10, 12, and 14 h. (b) Rietveld refined XRD pattern of $Ca_3Co_4O_9$ for 12 h sample.

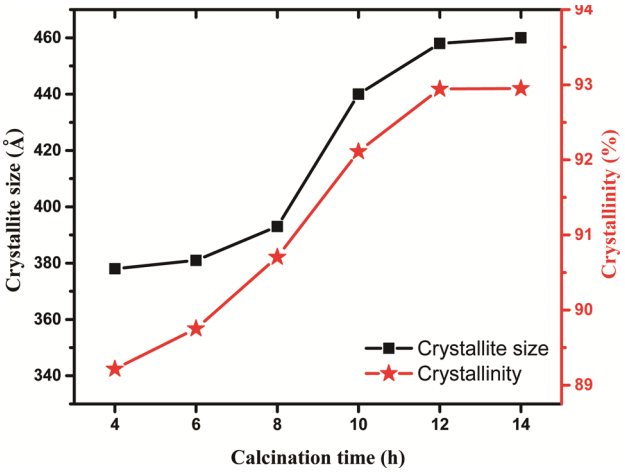

Fig. 7 Effect of calcination time on the crystallinity and crystallite size of $Ca_3Co_4O_9$ powder.

Table 1 Relevant parameters and reliability factors of $Ca_3Co_4O_9$ powder from XRD results calcinated at temperature 1073 K with different dwelling time (4, 6, 8, 10, 12, and 14 h)

Composition $Ca_3Co_4O_9$	Dwelling time (h)					
	4	6	8	10	12	14
Relevant parameters						
Crystal system	Monoclinic					
Crystallite size (nm)	37.8	38.1	39.3	44.0	45.8	46.0
Theoretical density (g/cm^3)	4.67	4.67	4.68	4.68	4.68	4.68
Volume (nm^3)	0.2365	0.2364	0.2364	0.2361	0.2365	0.2365
Lattice parameters						
A (nm)	0.4834	0.4829	0.4834	0.4833	0.4835	0.4836
$b_{Ca_2CoO_3}$ (nm)	0.4558	0.4554	0.4558	0.4552	0.4556	0.4557
b_{CoO_2} (nm)	0.2825	0.2822	0.2824	0.2821	0.2824	0.2824
b_1/b_2	1.6133	1.6135	1.6138	1.6134	1.6130	1.6136
c (nm)	1.0841	1.0857	1.0840	1.0843	1.0854	1.0858
α (°)	90	90	90	90	90	90
β (°)	98.126	98.121	98.176	98.181	98.173	98.158
γ (°)	90	90	90	90	90	90
Reliability factors						
R_{wp} (%)	4.68	4.38	4.23	4.20	4.18	4.16
R_p (%)	4.35	4.32	4.03	3.93	3.76	3.75
GOF	3.87	3.85	3.80	3.33	2.55	2.54

Based on the XRD results, it can be deduced that the highest purity of $Ca_3Co_4O_9$ powder is obtained at 1073 K for 12 and 14 h. Considering the energy consumption under these two conditions, 12 h is more favorable since their crystallite size and crystallinity are almost the same. Subsequently, the distribution of the elements on the microstructure of $Ca_3Co_4O_9$ powder at 1073 K for 12 h was characterized using EDS elemental mapping, and the results are shown in an overlay color image in Fig. 8(a). The measured EDX spectrum of $Ca_3Co_4O_9$ elements is illustrated in Fig. 8(b) with peaks of Ca, Co, and O, which verify the existence of Ca (24.9 wt%), Co (54.1 wt%), and O (20.7 wt%). Cobalt is homogeneously distributed in the investigated area, as shown in Fig. 8(c) with rose color. Identical distribution of calcium mapping element is represented in a light blue color, as shown in Fig. 8(d). The oxygen content is high and homogeneously distributed too, which referred by green color, as shown in Fig. 8(e). It can be said that from the SEM–EDS mapping, there were formations of an aggregate consisting of Co, Ca, and O. The quantitative of SEM–EDS analysis confirmed that the chemical compositions of the $Ca_3Co_4O_9$ sample corresponded to the nominal compositions. Furthermore, neither N nor C signals were detected in the EDS spectrum, which means the product is pure and free of any surfactant or impurity.

Figures 9(a)–9(e) show the structure observed for the as-calcined $Ca_3Co_4O_9$ powder at 1073 K for 12 h. It is noticed that the $Ca_3Co_4O_9$ particles appear as non-uniform size and shape, as shown in Fig. 9(a). Enlargement view of $Ca_3Co_4O_9$ particles is illustrated in Fig. 9(b). Darker contrast detected on the particles is attributable to metal-rich cobalt ion aggregates, bound with each other by the calcination process. High-resolution TEM images were obtained from the marked red square area Y in Fig. 9(b). The crystal layered structures of the material with distinct CoO_2 and Ca_2CoO_3 layers are clearly seen without lattice distortion defect. The atomic arrangement of Ca, Co, and O atoms are schematically presented next to high-resolution transmission electron microscopy (HRTEM) image in Fig. 9(d). This image is identical to the description of $Ca_3Co_4O_9$ crystal structure as described in Fig. 1. The d spacing of planes of $Ca_3Co_4O_9$ along the c direction is determined using Gatan software which is about 1.08 nm. This result is in agreement with the d spacing counted from the 00l peaks of the θ–2θ scan [6,14,18]. The selected area electron diffraction (SAED) patterns of the samples are

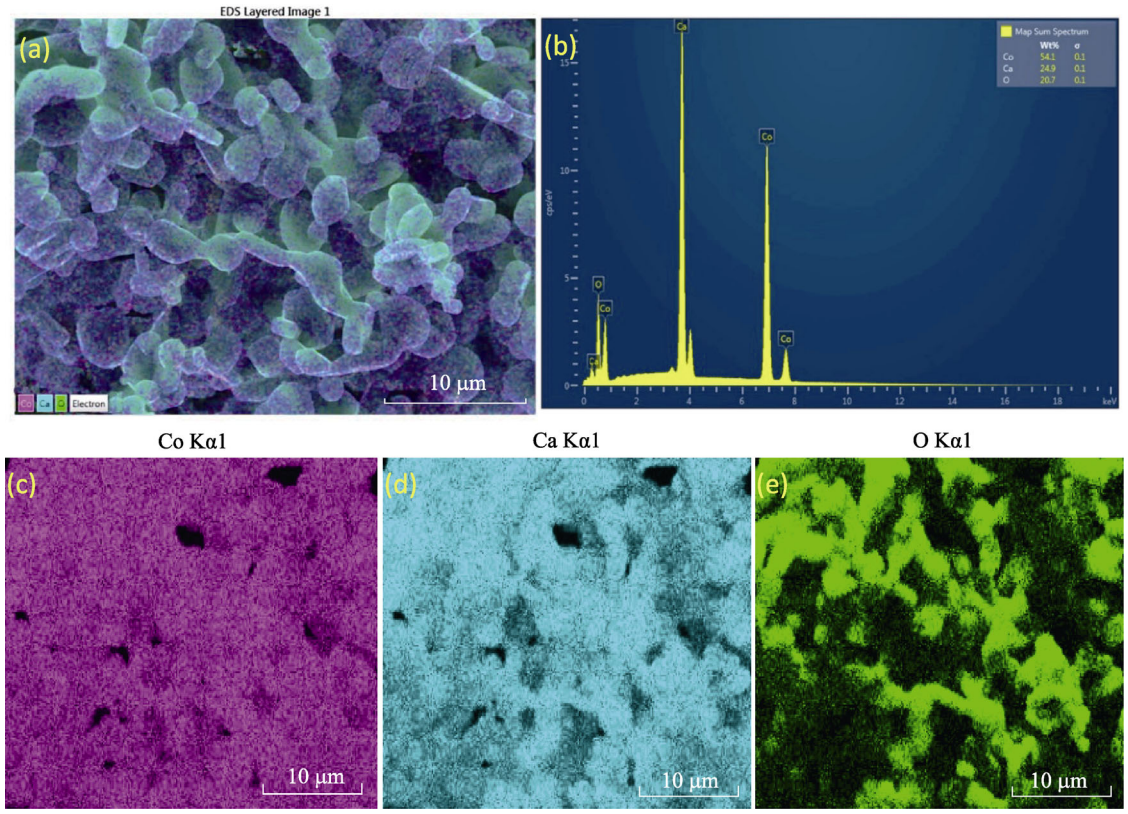

Fig. 8 SEM–EDS elemental mapping of $Ca_3Co_4O_9$ powder calcined at 1073 K for 12 h.

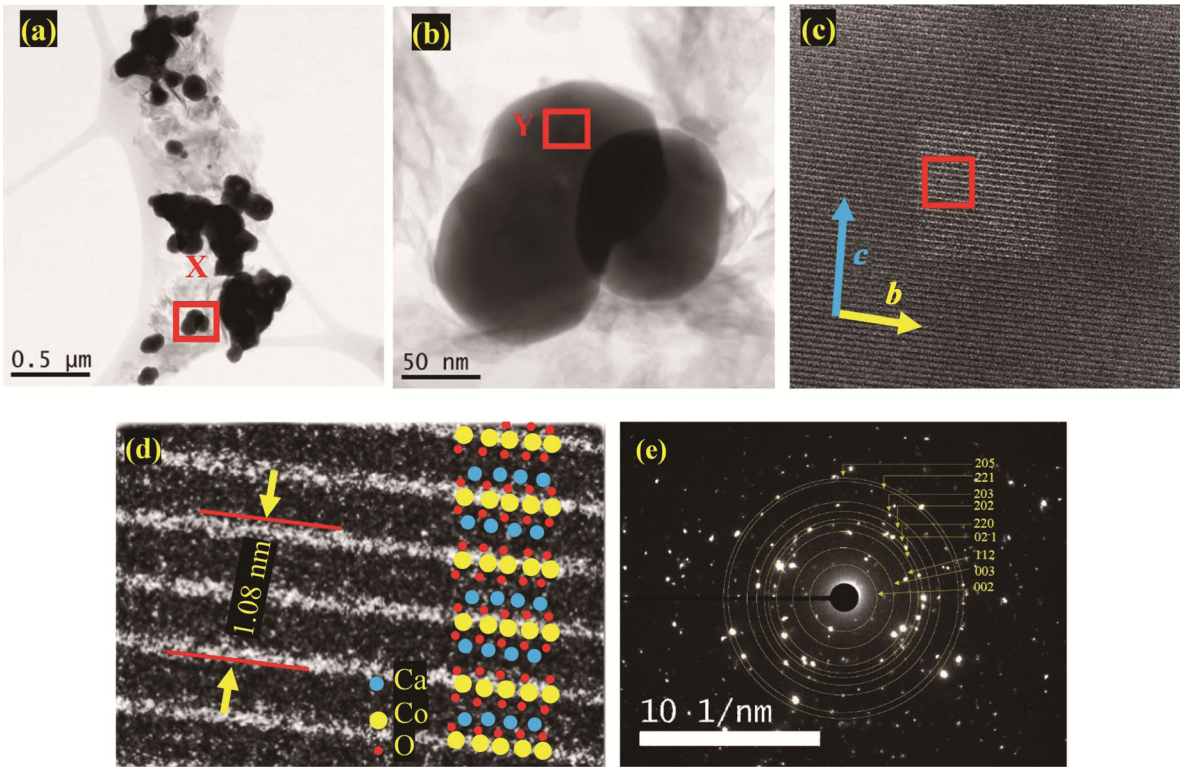

Fig. 9 TEM image of $Ca_3Co_4O_9$ structure with (a) low-magnification image, (b) enlargement of X-area, (c) enlargement of Y-area, (d) lattice-resolved TEM image and schematic of the atomic arrangement of the layers. (e) shows the SAED patterns recorded from the respective samples.

shown in Fig. 9(e). The samples had particle sizes in the order of several micrometers; therefore, the SAED covers the area, including small grains. The SAED shows diffraction spots of single crystals mixed with a speckled-ring pattern.

4 Conclusions

$Ca_3Co_4O_9$ is successfully synthesized using starch-assisted sol–gel auto-combustion method. The final powder is obtained through calcination at 1073 K by varying soaking time for 4, 6, 8, 10, 12, and 14 h. All the calcinated powder transforms into a single-phase calcium cobalt oxide with the particle size ranging from 1.15 to 1.47 μm. Similarly, the purity of calcium cobalt oxide particles increases with the increase of calcination time and becomes saturated after 12 h. TEM images also show no distinct lattice distortion defect observed on the crystal structure. The maximum attainable purity of $Ca_3Co_4O_9$ is 92.9%, which is a very encouraging result for the thermoelectric material applications. Besides the purity, the performance of thermoelectric material could be further enhanced via doping elements for improving their thermoelectric properties.

Acknowledgements

The authors would like to thank the Ministry of Education Malaysia (MOE), School of Mechanical Engineering, Faculty of Engineering, Institute for Vehicle Systems and Engineering and UTM Centre, Universiti Teknologi Malaysia (UTM), for Low Carbon Transport in cooperation with Imperial College London for providing the research facilities. This research study was supported by the Ministry of Education Malaysia (MOE) for the FRGS Grant (R.J130000. 7824.4F723) and Universiti Teknologi Malaysia (UTM) research grant (Q.J130000.2524.17H83).

References

[1] Zakharchuk KV, Tobaldi DM, Xiao XX, *et al*. Synergistic effects of zirconium- and aluminum co-doping on the thermoelectric performance of zinc oxide. *J Eur Ceram Soc* 2019, **39**: 1222–1229.

[2] Delorme F, Diaz-Chao P, Giovannelli F. Effect of Ca substitution by Fe on the thermoelectric properties of $Ca_3Co_4O_9$ ceramics. *J Electroceram* 2018, **40**: 107–114.

[3] Cha JS, Choi SM, Kim GH, *et al*. High-temperature thermoelectric properties of Sm^{3+}-doped $Ca_3Co_4O_{9+\delta}$ fabricated by spark plasma sintering. *Ceram Int* 2018, **44**: 6376–6383.

[4] Seo JW, Kim GH, Choi SM, *et al*. High-temperature thermoelectric properties of polycrystalline $CaMn_1$-Nb $O_{3-\delta}$. *Ceram Int* 2018, **44**: 9204–9214.

[5] Funahashi R, Matsubara I, Ikuta H, *et al*. An oxide single crystal with high thermoelectric performance in air. *Jpn J Appl Phys* 2000, **39**: L1127–L1129.

[6] Paul B, Schroeder JL, Kerdsongpanya S, *et al*. Mechanism of formation of the thermoelectric layered cobaltate $Ca_3Co_4O_9$ by annealing of CaO-CoO thin films. *Adv Electron Mater* 2015, **1**: 1400022.

[7] Chen S, Song XY, Chen XQ, *et al*. Effect of precursor calcination temperature on the microstructure and thermoelectric properties of $Ca_3Co_4O_9$ ceramics. *J Sol-Gel Sci Technol* 2012, **64**: 627–636.

[8] Torres MA, Costa FM, Flahaut D, *et al*. Significant enhancement of the thermoelectric performance in $Ca_3Co_4O_9$ thermoelectric materials through combined strontium substitution and hot-pressing process. *J Eur Ceram Soc* 2019, **39**: 1186–1192.

[9] Hira U, Han L, Norrman K, *et al*. High-temperature thermoelectric properties of Na- and W-doped $Ca_3Co_4O_9$ system. *RSC Adv* 2018, **8**: 12211–12221.

[10] Masset AC, Michel C, Maignan A, *et al*. Misfit-layered cobaltite with an anisotropic giant magnetoresistance: $Ca_3Co_4O_9$. *Phys Rev B* 2000, **62**: 166.

[11] Miyazaki Y, Onoda M, Oku T, *et al*. Modulated structure of the thermoelectric compound $[Ca_2CoO_3]_{0.62}CoO_2$. *J Phys Soc Jpn* 2002, **71**: 491–497.

[12] Królicka AK, Piersa M, Mirowska A, *et al*. Effect of sol-gel and solid-state synthesis techniques on structural, morphological and thermoelectric performance of $Ca_3Co_4O_9$. *Ceram Int* 2018, **44**: 13736–13743.

[13] Xu W, Butt S, Zhu YC, *et al*. Nanoscale heterogeneity in thermoelectrics: The occurrence of phase separation in Fe-doped $Ca_3Co_4O_9$. *Phys Chem Chem Phys* 2016, **18**: 14580–14587.

[14] Panchakarla LS, Lajaunie L, Ramasubramaniam A, *et al*. Nanotubes from oxide-based misfit family: The case of calcium cobalt oxide. *ACS Nano* 2016, **10**: 6248–6256.

[15] Prasoetsopha N, Pinitsoontorn S, Kamwanna T, *et al*. Thermoelectric properties of $Ca_3Co_{4-x}Ga_xO_{9+\delta}$ prepared by thermal hydro-decomposition. *J Electron Mater* 2014, **43**: 2064–2071.

[16] Miyazawa K, Amaral F, Kovalevsky AV, *et al*. Hybrid microwave processing of $Ca_3Co_4O_9$ thermoelectrics. *Ceram Int* 2016, **42**: 9482–9487.

[17] Sotelo A, Rasekh S, Madre MA, *et al*. Solution-based synthesis routes to thermoelectric $Bi_2Ca_2Co_{1.7}O_x$. *J Eur Ceram Soc* 2011, **31**: 1763–1769.

[18] Saini S, Yaddanapudi HS, Tian K, *et al*. Terbium ion doping in $Ca_3Co_4O_9$: A step towards high-performance

thermoelectric materials. *Sci Rep* 2017, **7**: 44621.

[19] Paul B, Lu J, Eklund P. Nanostructural tailoring to induce flexibility in thermoelectric $Ca_3Co_4O_9$ thin films. *ACS Appl Mater Interfaces* 2017, **9**: 25308–25316.

[20] Constantinescu G, Rasekh S, Torres MA, *et al*. Improvement of thermoelectric properties in $Ca_3Co_4O_9$ ceramics by Ba doping. *J Mater Sci: Mater Electron* 2015, **26**: 3466–3473.

[21] Diez JC, Torres MA, Rasekh S, *et al*. Enhancement of $Ca_3Co_4O_9$ thermoelectric properties by Cr for Co substitution. *Ceram Int* 2013, **39**: 6051–6056.

[22] Zhu T, Zhou JM. Effect of Ho doping on the high-temperature thermoelectric properties of $Ca_3Co_4O_9$-based oxides. *Adv Mater Res* 2011, **228–229**: 947–950.

[23] Vidyasagar K, Gopalakrishnan J, Rao CNR. A convenient route for the synthesis of complex metal oxides employing solid-solution precursors. *Inorg Chem* 1984, **23**: 1206–1210.

[24] Smaczyński P, Sopicka-Lizer M, Kozłowska K, *et al*. Low temperature synthesis of calcium cobaltites in a solid state reaction. *J Electroceram* 2007, **18**: 255–260.

[25] Bresch S, Mieller B, Selleng C, *et al*. Influence of the calcination procedure on the thermoelectric properties of calcium cobaltite $Ca_3Co_4O_9$. *J Electroceram* 2018, **40**: 225–234.

[26] Fey GTK, Cho YD, Prem Kumar T. A TEA-starch combustion method for the synthesis of fine-particulate $LiMn_2O_4$. *Mater Chem Phys* 2004, **87**: 275–284.

[27] Xu J, Wei CP, Jia K. Thermoelectric performance of textured $Ca_{3-x}Yb_xCo_4O_{9-\delta}$ ceramics. *J Alloys Compd* 2010, **500**: 227–230.

[28] Katsuyama S, Takiguchi Y, Ito M. Synthesis of $Ca_3Co_4O_9$ ceramics by polymerized complex and hydrothermal hot-pressing processes and the investigation of its thermoelectric properties. *J Mater Sci* 2008, **43**: 3553–3559.

[29] Zhang YF, Zhang JX, Lu QM, *et al*. Synthesis and characterization of $Ca_3Co_4O_9$ nanoparticles by citrate sol-gel method. *Mater Lett* 2006, **60**: 2443–2446.

[30] Presečnik M, de Boor J, Bernik S. Synthesis of single-phase $Ca_3Co_4O_9$ ceramics and their processing for a microstructure-enhanced thermoelectric performance. *Ceram Int* 2016, **42**: 7315–7327.

[31] Park K, Hakeem DA, Cha JS. Synthesis and structural properties of thermoelectric $Ca_{3-x}Ag_xCo_4O_{9+\delta}$ powders. *Dalton Trans* 2016, **45**: 6990–6997.

[32] Romo-De-la-cruz C, Liang L, Navia SAP, *et al*. Role of oversized dopant potassium on the nanostructure and thermoelectric performance of calcium cobaltite ceramics. *Sustainable Energy Fuels* 2018, **2**: 876–881.

[33] Kahraman F, Madre MA, Rasekh S, *et al*. Enhancement of mechanical and thermoelectric properties of $Ca_3Co_4O_9$ by Ag addition. *J Eur Ceram Soc* 2015, **35**: 3835–3841.

[34] Yang WC, Qian HJ, Gan JY, *et al*. Effects of Lu and Ni substitution on thermoelectric properties of $Ca_3Co_4O_{9+\delta}$. *J Elec Mater* 2016, **45**: 4171–4176.

[35] Tang GD, Yang WC, He Y, *et al*. Enhanced thermoelectric properties of $Ca_3Co_4O_{9+\delta}$ by Ni, Ce co-doping. *Ceram Int* 2015, **41**: 7115–7118.

[36] Butt S, Xu W, He WQ, *et al*. Enhancement of thermoelectric performance in Cd-doped $Ca_3Co_4O_9$ via spin entropy, defect chemistry and phonon scattering. *J Mater Chem A* 2014, **2**: 19479–19487.

[37] Yadav RS, Havlica J, Hnatko M, *et al*. Magnetic properties of $Co_{1-x}Zn_xFe_2O_4$ spinel ferrite nanoparticles synthesized by starch-assisted sol–gel autocombustion method and its ball milling. *J Magn Magn Mater* 2015, **378**: 190–199.

[38] Singh Yadav R, Havlica J, Masilko J, *et al*. Effects of annealing temperature variation on the evolution of structural and magnetic properties of $NiFe_2O_4$ nanoparticles synthesized by starch-assisted sol–gel auto-combustion method. *J Magn Magn Mater* 2015, **394**: 439–447.

[39] Motevalian A, Salem S. Effect of glycine-starch mixing ratio on the structural characteristics of $MgAl_2O_4$ nano-particles synthesized by sol-gel combustion. *Particuology* 2016, **24**: 108–112.

[40] Dinh TT, Nguyen TQ, Quan GC, *et al*. Starch-assisted sol–gel synthesis of magnetic $CuFe_2O_4$ powder as photo-Fenton catalysts in the presence of oxalic acid. *Int J Environ Sci Technol* 2017, **14**: 2613–2622.

[41] Ansari F, Sobhani A, Salavati-Niasari M. Simple sol-gel synthesis and characterization of new $CoTiO_3/CoFe_2O_4$ nanocomposite by using liquid glucose, maltose and starch as fuel, capping and reducing agents. *J Colloid Interface Sci* 2018, **514**: 723–732.

[42] M A M, Sudin I, Mohd Noor A, *et al*. Investigation on microstructure and electrical properties of Bi doping $Ca_3Co_4O_9$ nanoparticles synthesized by sol-gel process. *Int J Eng Technol* 2018, **7**: 31.

[43] Ene CD, Patrinoiu G, Munteanu C, *et al*. Multifunctional ZnO materials prepared by a versatile green carbohydrate-assisted combustion method for environmental remediation applications. *Ceram Int* 2019, **45**: 2295–2302.

[44] Visinescu D, Tirsoaga A, Patrinoiu G, *et al*. Green synthetic strategies of oxide materials: Polysaccharides-assisted synthesis. *Rev Roum Chim* 2010, **55**: 1017–1026.

[45] Agilandeswari K, Ruban Kumar A. Synthesis, characterization, temperature dependent electrical and magnetic properties of $Ca_3Co_4O_9$ by a starch assisted sol–gel combustion method. *J Magn Magn Mater* 2014, **364**: 117–124.

[46] Zhang DB, Zhang BP, Ye DS, *et al*. Enhanced Al/Ni co-doping and power factor in textured ZnO thermoelectric ceramics prepared by hydrothermal synthesis and spark plasma sintering. *J Alloys Compd* 2016, **656**: 784–792.

[47] Han L, van Nong N, Zhang W, *et al*. Effects of morphology on the thermoelectric properties of Al-doped ZnO. *RSC Adv* 2014, **4**: 12353.

[48] Khorsand Zak A, Abd Majid WH, Mahmoudian MR, *et al*.

Starch-stabilized synthesis of ZnO nanopowders at low temperature and optical properties study. *Adv Powder Technol* 2013, **24**: 618–624.

[49] Ahmad K, Wan C, Al-Eshaikh MA, *et al*. Enhanced thermoelectric performance of Bi_2Te_3 based graphene nanocomposites. *Appl Surf Sci* 2019, **474**: 2–8.

[50] Zhu HY, Su TC, Li HT, *et al*. Thermoelectric properties of BiCuSO doped with Pb. *Solid State Commun* 2018, **278**: 1–5.

[51] Yu HB, Wang XP, Li Y. Strong impact of cobalt distribution on the activity for $Co_3O_4/CaCO_3$ catalyzing N_2O decomposition. *Catal Today* 2020, **339**: 274–280.

[52] Qi XL, Fan YY, Zhu DS, *et al*. Fabrication and characterization of $Ca_3Co_4O_9$ nanoparticles by sol-gel method. *Rare Met* 2011, **30**: 111–115.

[53] Petříček V, Dušek M, Palatinus L. Crystallographic computing system JANA2006: General features. *Zeitschrift Für Kristallographie-Cryst Mater* 2014, **229**: 345–352.

[54] Lambert S, Leligny H, Grebille D. Three forms of the misfit layered cobaltite $[Ca_2CoO_3][CoO_2]_{1.62}$·A 4D structural investigation. *J Solid State Chem* 2001, **160**: 322–331.

[55] Asahi R, Sugiyama J, Tani T. Electronic structure of misfit-layered calcium cobaltite. *Phys Rev B* 2002, **66**: 155103.

[56] Grebille D, Lambert S, Bourée F, *et al*. Contribution of powder diffraction for structure refinements of aperiodic misfit cobalt oxides. *J Appl Cryst* 2004, **37**: 823–831.

[57] Rahnamaeiyan S, Talebi R. Preparation and characterization of the bismuth aluminate nanoparticles via a green approach and its photocatalyst application. *J Mater Sci: Mater Electron* 2016, **27**: 304–309.

[58] Agilandeswari K, Saral AM, Kumar AR. Magnetic, optical, microscopic and electrical behavior of $Ca_{2-x}Y_xCo_2O_5$ prepared by a molten flux method. *Mater Sci Semicond Process* 2015, **34**: 205–213.

[59] Rahnamaeiyan S, Talebi R. Preparation and characterization of the bismuth aluminate nanoparticles via a green approach and its photocatalyst application. *J Mater Sci: Mater Electron* 2016, **27**: 304–309.

[60] Zhao KP, Duan HZ, Raghavendra N, *et al*. Solid-state explosive reaction for nanoporous bulk thermoelectric materials. *Adv Mater* 2017, **29**: 1701148.